pubs.acs.org/estair

Article

Chemical Imaging of Atmospheric Biomass Burning Particles from North American Wildfires

Published as part of ACS ES&T Air special issue "Wildland Fires: Emissions, Chemistry, Contamination, Climate, and Human Health".

Felipe A. Rivera-Adorno, Jay M. Tomlin, Nurun Nahar Lata, Lisa Azzarello, Michael A. Robinson, Rebecca A. Washenfelder, Alessandro Franchin, Ann M. Middlebrook, Swarup China, Steven S. Brown, Cora J. Young, Matthew Fraund, Ryan C. Moffet, and Alexander Laskin*

Cite This: ACS EST Air 2025, 2, 508−521

Read Online

ACCESS | Metrics & More | Article Recommendations | Supporting Information

ABSTRACT: The effects of biomass burning aerosols (BBA) on radiative forcing and cloud formation depend on chemical composition and the internal structures of individual particles within smoke plumes. To improve our understanding of the chemical and physical properties of BBA emitted at different times of the day and their evolution during atmospheric aging, we conducted a study as a part of the Fire Influence on Regional to Global Environments and Air Quality field campaign. Particle samples were collected onboard a research aircraft from smoke plumes from a wildfire in eastern Oregon during late afternoon and nighttime flights on August 28, 2019. A time-resolved aerosol collector was used to collect samples on substrates for offline spectromicroscopic imaging to investigate the single-particle characteristics of BBA particles. Approximately 20,400 individual particles from 10 selected samples were analyzed using computer-controlled scanning electron microscopy coupled with energy-dispersive X-ray microanalysis, revealing their elemental composition, morphology, and viscosity. Elemental microanalysis indicated that aged potassium is likely found in the form of K_2SO_4, KNO_3, and possible K-organic salts. Further chemical speciation and carbon bonding mapping within individual particles were conducted using synchrotron-based scanning transmission X-ray microscopy (STXM) coupled with near edge X-ray absorption fine structure (NEXAFS) spectroscopy. Real-time, water-soluble light absorption measurements were acquired using a particle-into-liquid sampler instrument coupled to a liquid waveguide capillary cell and total organic analyzer. In the late afternoon samples, 65% of the total particle number population consisted entirely of organic components, compared to 46% in the nighttime particles. These differences were attributed to discrepancies in composition at the time of emission and to the daytime condensation and accumulation of photochemically formed secondary organic material on existing BBA particles, a process that halts at night. Microscopy images indicated that particle viscosity was lower in the nighttime particles ($<10^1$ Pa·s), likely due to increased relative humidity and a higher contribution from hygroscopic inorganic components. The chemical heterogeneity of individual particles was quantified using STXM-derived mixing state parameters. The nature of carbon bonding within individual particles was inferred from the extent of carbon sp^2 hybridization derived from NEXAFS spectra. Average percentages of sp^2 hybridization range between 40% and 60%, with no noticeable differences between late afternoon and nighttime flights. These findings were compared with the online optical properties of both late afternoon and nighttime smoke plumes, providing valuable insights into the complex relationship between chemical composition and optical properties of BBA particles at different times of the day.

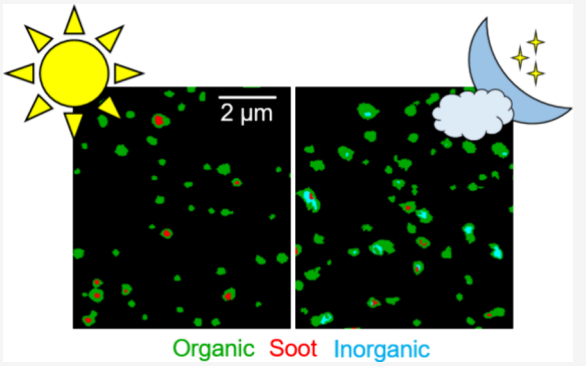

KEYWORDS: *atmospheric particles, chemical imaging, electron microscopy, X-ray microscopy, particle mixing state, biomass burning emissions*

INTRODUCTION

In recent decades, climate change has driven an increase in the area burned during wildfire events across different regions, largely as a result of extended meteorological droughts and heightened fire weather conditions.[1] Wildland fires, including both forest fires and prescribed burns, are a significant source of atmospheric biomass burning aerosols (BBA). These

Received: September 9, 2024
Revised: March 20, 2025
Accepted: March 21, 2025
Published: April 1, 2025

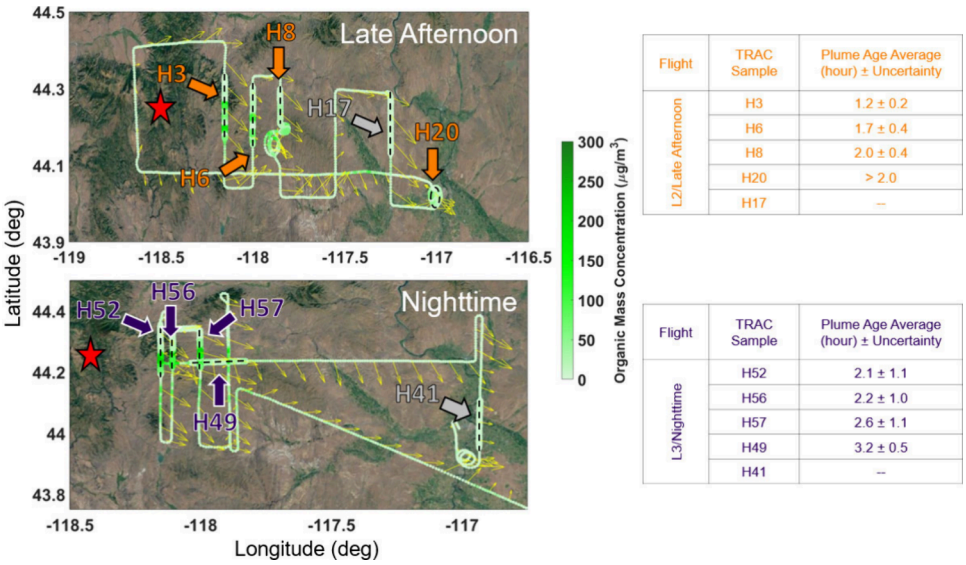

Flight	TRAC Sample	Plume Age Average (hour) ± Uncertainty
L2/Late Afternoon	H3	1.2 ± 0.2
	H6	1.7 ± 0.4
	H8	2.0 ± 0.4
	H20	> 2.0
	H17	--

Flight	TRAC Sample	Plume Age Average (hour) ± Uncertainty
L3/Nighttime	H52	2.1 ± 1.1
	H56	2.2 ± 1.0
	H57	2.6 ± 1.1
	H49	3.2 ± 0.5
	H41	--

Figure 1. Late afternoon (top) and nighttime (bottom) flight tracks showing aerosol organics concentrations measured by AMS and wind directions (yellow arrows). Larger data points, dashed lines, and markers highlight in-plume (orange/dark purple) and background (gray) samples collected with the TRAC and selected for further chemical imaging. Star shows location of the 204 Cow wildfire. Time periods of both flights are 16:24−18:37 (late afternoon) and 19:32−22:07 (nighttime) reported as local time (PDT). No plume age was reported for background samples H17 and H41.

aerosols have a direct impact on regional and global climate by scattering and absorbing solar radiation.[2,3] Additionally, BBA particles indirectly affect climate by altering cloud formation, physicochemical properties, and lifecycle.[4,5] BBA particles also have significant impacts on air quality, visibility, and human health, especially in densely populated areas near the expanding wildland-urban interface.[6−12] Despite their importance, atmospheric models often struggle to adequately account for the variability in the chemical and optical properties among BBA particles, leading to ambiguity in accounting for their atmospheric processes and impact.

BBA particles consist of those directly emitted from the source, such as primary organic aerosols (POA), inorganic salts, and soot, as well as secondary organic aerosol (SOA) formed through condensation of oxidized volatile organic compounds (VOCs).[13−15] Typically, particles within the smoke plume exhibit multicomponent internal composition, where particle cores are often composed of soot/elemental carbon (EC) or inorganic salts, with a coating of organic carbon (OC).[16−20] The composition and properties of BBA particles vary based on the type of fuel and burning conditions at the source, which affect combustion efficiency.[21−25] The effects of daytime photochemistry versus nighttime dark conditions further complicate the mechanisms and yields of SOA formation.[26−28] Therefore, characterization of BBA particles and quantification of their impact on climate, air quality, and health present significant technical and scientific challenges, necessitating a combination of online and offline studies.

Aircraft-based field studies have been employed to investigate properties of smoke plume particles during both daytime and nighttime wildfire events in the western United States.[28−30] Airborne measurement platforms offer significant advantages, as aircraft can track smoke plumes along semi-Lagrangian trajectories, enabling dynamic studies of aerosol emission and evolution. Real-time measurements onboard aircraft can determine particle size distribution,[31] composition,[32−34] and light absorption of BBA smoke plumes in the atmosphere.[35−37] These observations are crucial for developing more accurate atmospheric and climate models and implementing relevant mitigation strategies. However, online methods are often limited to bulk analysis and neglect variations in the chemical and light-absorbing properties between individual BBA particles. Achieving a more comprehensive understanding of BBA emission and evolution requires combining online measurements with offline single particle analysis. Techniques commonly used to study individual BBA particles include computer-controlled scanning electron microscopy coupled with energy dispersive X-ray spectroscopy (CCSEM/EDX) and scanning transmission X-ray microscopy coupled with near-edge X-ray absorption fine structure (STXM/NEXAFS) spectroscopy.[38] CCSEM/EDX microanalysis is used to probe the size, morphological metrics and elemental composition of collected BBA particles.[39−41] STXM/NEXAFS spectroscopy distinguishes between components of OC, EC, and inorganics (IN), while also providing spatially resolved chemical imaging of carbon bonding and oxidation states.[19,20,42−44] Consequently, the combination of CCSEM/EDX and STXM/NEXAFS spectroscopy has become a method of choice for offline chemical imaging of BBA particles,[21,43,45,46] offering detailed insights into their complex chemical and physical properties.

In this study, we conducted spectromicroscopy chemical imaging of BBA particles collected onboard the NOAA Twin Otter aircraft during the 2019 Fire Influence on Regional to Global Environments and Air Quality (FIREX-AQ) field campaign.[47] Our objective was to offer a comprehensive understanding of the single-particle properties of BBA. Real-time bulk chemical composition data was used to identify points of interest within the smoke plume. Substrate samples collected during late afternoon and nighttime flights were subsequently probed using offline CCSEM/EDX and STXM/NEXAFS. These advanced techniques provided detailed physicochemical characterization of BBA particles and revealed

https://doi.org/10.1021/acsestair.4c00242
ACS EST Air 2025, 2, 508−521

the distribution of their OC, EC, and IN components. The extent of carbon bond hybridization, derived from STXM/NEXAFS, was quantified and further compared with in situ optical measurements. The insights gained from this study contribute to a better understanding of BBA particle properties, which can inform atmospheric modeling predictions related to air quality, visibility, and climate impact.

METHODS

Aircraft Measurement Platform. This report describes observations from two flights on August 28, 2019, as a part of the FIREX-AQ airborne field campaign.[47] These flights, designated as L2 (late afternoon: 16:24−18:37 PDT) and L3 (nighttime L3:19:32−22:07 PDT), focused on contrasting the chemical imaging data of individual BBA particles collected aboard the NOAA Twin Otter research aircraft. The flights sampled wildfire smoke plumes, identified by significant carbon monoxide (CO) enhancements, and followed flight trajectories that included at least three downwind plume transects.[36] Figure 1 illustrates the flight paths downwind of the 204 Cow wildfire, which began on August 9, 2019, approximately 27.4 km southwest of Unity, Oregon (initial wildfire coordinates: 44.2851, −118.4598). 3D versions of the flight maps are provided in Figure S1, with data points color-coded to represent mass concentrations of condensed-phase organics measured with a high-resolution time-of-flight aerosol mass spectrometer (HR-ToF-AMS, Aerodyne Research Inc., Billerica, MA, USA).[35] To facilitate the chemical analysis of the smoke plume during atmospheric aging, the aircraft began sampling near to the emission source and then conducted a sequence of downwind transects at increasing distances from the fire. This approach, combined with the flight speed (65−75 m s^{-1}), enabled near-Lagrangian data acquisition and sampling of BBA particles.[36] The aircraft payload included an ultrahigh sensitivity aerosol spectrometer (UHSAS) particle counter for measuring particle diameter (0.07−1 μm) and number concentrations.[28,48] In order to reduce coincidence corrections for large number of particles within the smoke plumes, the UHSAS sample stream was diluted as needed during data acquisition. The magnitude of the dilution ratio was not precise, so the UHSAS total volume concentrations were scaled with the HR-AMS data. This dilution likely affected the particle size distributions by evaporation of semivolatile components. Hence, comparisons of the UHSAS particle size distributions with the electron microscopy particle size distributions here are qualitative. A PILS instrument coupled to a liquid waveguide capillary cell and total organic analyzer was used to determine the light absorption by "brown carbon" (BrC) components of water soluble organic carbon (WSOC) in BBA within a wavelength range of 310−500 nm (BrC-PILS hereafter).[35−37]

Sample Collection for Offline Chemical Imaging. Sequential sampling was carried out during both flights using an automated time-resolved aerosol collector (TRAC)[49] operated at a flow rate of 1 L min^{-1}, with each sample collected for 4 min. The aerodynamic cutoff size (D_{50}) for the TRAC is 0.36 μm. Copper 400 mesh transmission electron microscopy (TEM) grids coated with Carbon Type-B films (Ted Pella, Inc.) were used for sample collection and subsequent analysis. Samples were collected continuously throughout both flights. Samples for spectromicroscopic chemical imaging were selected based on several criteria: the AMS organic mass concentrations (Figure S2), the sample location within the flight trajectory (one sample per plume crossing), and calculated smoke plume ages. TRAC sampling coverage described here was similar but not identical to individual plume transects of the maximum smoke concentrations analyzed for a complementary study.[35] In total, five samples were selected for each flight, both within the plume and from background air. The smoke plume age was estimated using high-resolution meteorological data sets, including the High-Resolution Rapid Refresh, North American Mesoscale Forecast System CONUS Nest, and the Global Forecast System.[36] The ages and uncertainties of individual late afternoon and nighttime samples are listed in Figure 1 and Table S1.

Chemical Imaging of Sampled Particles. Size, morphology, and elemental composition of individual particles were examined using CCSEM/EDX (FEI Quanta 3D, EDAX Genesis).[43] The instrument was operated at an accelerating voltage of 20 kV and beam current of 430 pA. The relative atomic fractions of the 15 most common elements (C, N, O, Na, Mg, Al, Si, P, S, Cl, K, Ca, Mn, Fe, and Cu) were quantified for each particle. The Cu EDX peak is heavily influenced by a background signal from the TEM substrate and the mounting plate (made of a beryllium−copper alloy). Therefore, quantified atomic fractions of Cu were excluded from the particle-type classification algorithm. *K*-means clustering analysis was implemented on 20,382 particles analyzed in ten samples to classify the particle types based on their elemental composition.[50−53] The per-sample statistics are listed in Table S2. This classification allowed us to determine the contribution of each particle type within individual samples from both flights. To assess the viscosity of individual substrate-impacted particles, their height-to-width (H/W) ratios were measured using SEM images acquired at 80° tilt angle.[54] These measurements were performed manually using ImageJ software 1.52a (http://imagej.net/ij, Java1.8.0_112).

The carbon content of particles was analyzed using a synchrotron-based STXM/NEXAFS instrument operated at carbon K-edge energies (278−320 eV). This technique enabled the mapping of OC, EC, and IN components within individual particles, as well as the spectroscopic detection of OC functional groups.[38,43,46,52,53,55−57] The STXM data acquisition was performed by raster-scanning a focused field-of-view at selected X-ray energies. The light transmitted through each pixel of the sample is detected and converted to spatially resolved optical depth at X-ray energy E (OD_E), calculated using the Beer−Lambert Law:

$$OD_E = -\ln\left(\frac{I(E)}{I_0(E)}\right) = \mu(E)\rho t \quad (1)$$

where I and I_0 represent the X-ray intensities transmitted through the sample and background regions, respectively; μ is the mass absorption coefficient of the material, derived from its elemental composition and optical cross section provided by Henke tables;[58] ρ is the density; and t is the optical thickness of the specimen. Carbon "maps" were acquired at four specific energies to differentiate between OC, EC, and IN over large ensembles of particles.[55] More detailed chemical information was obtained by measuring OD_E at 96 X-ray energies during carbon "stacks" acquisition, yielding a full NEXAFS spectrum for each imaged pixel. A total of 4,942 particles were analyzed using STXM/NEXAFS across all samples (Table S2). The

https://doi.org/10.1021/acsestair.4c00242
ACS EST Air 2025, 2, 508−521

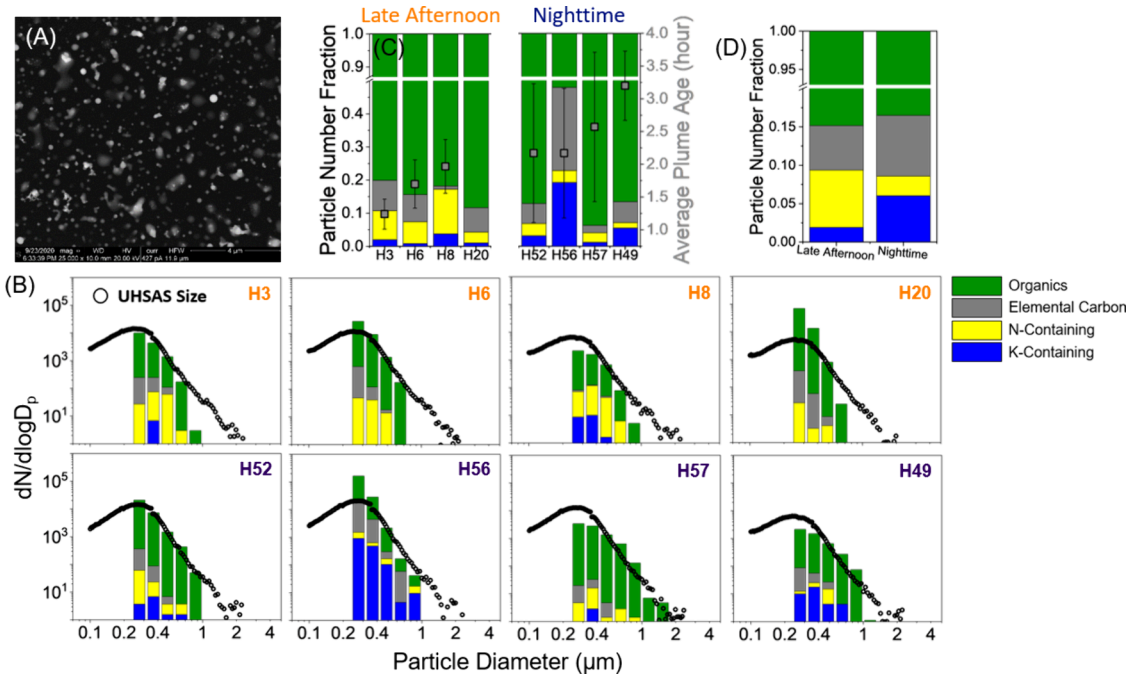

Figure 2. (A) Representative SEM image of BBA particles from sample H3. (B) PSD acquired from CCSEM/EDX chemical imaging compared to UHSAS size measurements; two data sets are superimposed and anchored at 0.50 μm to facilitate visual comparison. Panels are arranged left-to-right to reflect increasing plume age and aerosol evolution in the late afternoon and nighttime, respectively. (C) Normalized relative contribution of particle-type clusters in individual samples as a function of plume age, with error bars indicating uncertainty in plume age calculations. (D) Relative contribution of particle-type clusters, reported as a fraction of the total particle population, representative of late afternoon and nighttime smoke plumes.

maps and stacks were acquired with a spatial resolution of 35–40 nm, sufficient for describing internal and external mixing states of submicron ambient particles. A detailed description of STXM/NEXAFS measurements and definitions of the main chemical components is included in Supporting Information, Note 3.

Particle Organic Volume Fractions, Particle Hygroscopicity, and Mixing State Parameterization. STXM maps were utilized to calculate the organic volume fractions (OVF) of individual BBA particles. The calculation method involves computing the thickness of the OC, IN, and EC components within each particle, following methodologies established in previous studies.[55,56] Detailed information on OVF calculations from STXM measurements are included in Supporting Information, Note 4. The OVF values obtained from STXM data were then used to estimate water uptake characteristics of individual particles. The aerosol hygroscopicity κ parameter[59] was determined for mixed organic–inorganic particles using the following equation:

$$\kappa = (1 - \mathrm{OVF})\kappa_{\mathrm{inorg}} + \mathrm{OVF}\kappa_{\mathrm{org}} \quad (2)$$

where κ_{inorg} and κ_{org} represent the hygroscopicity parameters for the inorganic and organic components, respectively. For the inorganic component, $\kappa_{\mathrm{inorg}} = 0.9$, corresponds to KCl,[60] while the organic component, $\kappa_{\mathrm{org}} = 0.06$, corresponds to organic BBA.[61] In this study, κ represents relative water uptake activity of BBA assuming a binary system of representative organic and inorganic species, and does not account for discrepancies in hygroscopicity between organic species with different oxidation states. While soot contributes to the calculation of OVF, it is excluded in eq 2, as its hydrophobic nature accounts for a negligible fraction of the water-uptake characteristics of particles.

The chemical diversity of the sampled BBA particles was quantified using mixing state metrics[62] adapted for STXM applications, using the mass fractions of three principal components: OC, EC, and IN.[46] A detailed summary of these entropy-based mixing state parametrizations is included in Supporting Information, Note 5. These metrics are essential for evaluating the extent to which individual particles represent the bulk composition, allowing for the distinction between internally and externally mixed particles.

RESULTS AND DISCUSSION

Elemental Microanalysis of Individual BBA Particles. The *k*-means clustering results, summarized in Figure S4, illustrate the composition of individual clusters as mean elemental spectra representative of each group, with the particle-specific elemental information presented in Figure S5. Clusters were defined from CCSEM/EDX measurements using the cluster centroid values with elements greater than 0.5%. Cluster #1 (Organics) accounts for approximately 85% (17,376 particles) of the total particle load and is attributed to POA and SOA particles, based on the absence of all elements other than carbon and oxygen. Cluster #2 (K-containing), accounting only for 2.4% (483 particles), exhibits the most diverse particle composition, which includes additional elements such as potassium (K), calcium (Ca), sulfur (S), among others. In fresh BBA emissions, KCl is commonly reported as a K-bearing salt.[18,19,63–66] However, a manual inspection of individual K-containing particles over longer EDX acquisition times revealed their elemental associations predominantly with sulfur, while only trace levels of Cl observed, as illustrated in Figure S6. This finding suggests that

https://doi.org/10.1021/acsestair.4c00242
ACS EST Air 2025, 2, 508–521

K_2SO_4, KNO_3, and K-organics are likely the dominant K-bearing salts. These compounds form in aged particles, where KCl has undergone atmospheric processing through acid-displacement reactions.[64,67,68] Cluster #3 (N-containing), which accounts for 3.5% (704 particles), shows a significant nitrogen contribution in addition to carbon and oxygen. Although nitrogen quantification by EDX is inaccurate, its qualitative presence in BBA particles suggests contributions from ammonium, nitrates, and N-containing organics, aligning with AMS-derived mass concentrations of NH_4^+ and NO_3^- salts.[35] Cluster #4 (Elemental Carbon), representing 9% (1,819 particles), includes particles with the dominant signal from carbon, indicating EC composition. Of note, the sensitivity of EDX toward oxygen is limited. Hence, cluster #4 potentially represents a combination of graphitic soot and amorphous organics with low oxygen content.

A typical SEM image of particles collected during the late afternoon is shown in Figure 2A, with additional SEM images representing all in-plume samples provided in Figure S8. Consistent with previous studies, our BBA samples exhibit a complex distribution of particles with diverse morphologies.[19,69−71] Figure 2B presents 8-bin/decade particle size distributions (PSD) for the in-plume samples collected during the late afternoon (H3, H6, H8, and H20) and the nighttime (H49, H52, H56, and H57) flights, along with size-resolved contributions from each cluster. To facilitate a visual comparison between PSDs inferred from CCSEM and UHSAS measurements, the CCSEM data were scaled to particle size measurements by converting mobility diameter to aerodynamic diameter, which corresponds to MOUDI sampling. While this conversion method requires known metrics of particle dynamic shape factors, settling velocity, and density,[72] we only utilized the particle density which was assumed to be 1.4 g/cm^3, as previously discussed for biomass burning events.[43] PSDs inferred from CCSEM and UHSAS measurements were superimposed and anchored at 0.50 μm to facilitate visual comparison across the panels of Figure 2B, which depict size-resolved chemical composition. This alignment is necessary because the chemical imaging techniques provide only relative fractions of the analyzed particles. Figure 2C displays the normalized average contribution of each particle-type population relative to the total particle counts in late afternoon and nighttime samples, along with the estimated plume ages (plume age was not calculated for sample H20 because the sample was obtained as the plane flew up then down in a spiral for landing). The contribution of the *Organics* cluster #1 in late afternoon samples ranges from 80 to 88%. While a slight increase in the fraction of particles in the organics cluster is observed at later plume ages, the differences between corresponding transects are not significant. Thus, comparing combined samples where particles for each category were added together from each of the two flights offers more significant insights into BBA particle composition and the temporal variations of the aging smoke plume. Figure 2D shows the contribution of each cluster with respect to late afternoon versus nighttime particle populations. While differences in *Organics* cluster #1 between both flights are not substantial, the contribution of the *K-containing* cluster #2 with respect to the total particle population is smaller during the late afternoon (2%) compared to night samples (6%). The average fraction of elemental carbon particles in cluster #4 is also higher for the nighttime samples. Discrepancies are also observed between both flights for cluster #3, with *N-containing* particles contributing more significantly during the late afternoon (7%) compared to the nighttime (3%). Despite noticeable differences in cluster #3, these findings are semiquantitative due to the limited reliability of EDX microanalysis for low-Z elements < Na.[50,73] The uncertainties in the *k*-means clustering, as determined through Silhouette analysis of the reported cluster populations, reveal that approximately half of the particles in the *K-containing* cluster #2 exhibit compositional characteristics significantly deviating from the cluster centroid values, as shown in Figure S7. This finding reflects the complexity and high variability of the EDX spectra recorded for particles within this cluster.

The differences between the late afternoon and nighttime samples may be influenced by sample H56, which contains the highest fraction of *K-containing* particles with significant variability between them. This sample was obtained over the same time as the plume transect with an age of 2.4 h analyzed in the complementary study.[35] This smoke plume transect had the highest ratio of the AMS organic mass to carbon monoxide (171 μg m^{-3}) and the lowest AMS average oxidation state of carbon (−0.72) for all transects measured on that day. It was also the nighttime transect with the highest AMS organic mass fraction and the lowest AMS ammonium mass fraction. As shown below, there were other differences noted from this sample compared to the others obtained on the nighttime flight. Thus, this particular smoke transect was unique in several ways.

The results described here are based on classifying individual particles into four distinct clusters. A comparison of these results directly with dilution-corrected mass concentrations, as reported in our complementary study on the same flights,[35] should be considered qualitative. While the real-time aerosol composition data reported by the AMS revealed changes or stability in aerosol composition as a function of plume age, no corresponding trends were apparent in the CCSEM data. Furthermore, the AMS is not sensitive to potassium salts (cluster #2) or elemental carbon (cluster #4), both of which were inferred from the X-ray microanalysis. As a result, systematic comparisons between AMS data of the bulk composition and the single-particle analysis performed using CCSEM/EDX and STXM/NEXAFS, are not feasible. Nonetheless, chemical imaging techniques provide invaluable per-particle information on refractory chemical species that are not quantified by AMS, including KCl, soot, and mineral dust.

Assessment of Particle Viscosity. Previous studies have shown that airborne particles undergo morphological changes when collected by impaction.[74,75] Highly viscous and semisolid particles retain their shape and size upon impact, whereas liquid-like particles flatten. The viscosity of particles deposited on substrates can be estimated from their height-to-width (H_{obs}/W) ratios,[54] which can be assessed using SEM images taken at tilted angle, as shown in Figure S9. This approach assumes that observed particles are mostly organic and their inorganic components have only minor effects on their observed height-to-width ratios. In our study, the late afternoon samples displayed a wide variation of particle morphologies, including spherical, dome-like, and flat particles with broad range of H_{obs}/W ratios. In contrast, nighttime samples were dominated by liquid-like flat particles. Figure 3 presents the H_{obs}/W ratios measured for ensembles of individual particles, which were used to estimate particle viscosity based on our recently reported approach.[54] The late afternoon samples were dominated by semiviscous (10^4−10^8

https://doi.org/10.1021/acsestair.4c00242
ACS EST Air 2025, 2, 508−521

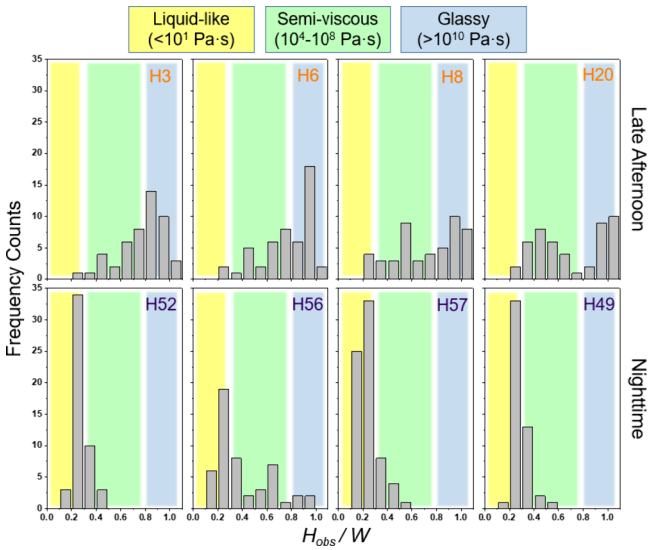

Figure 3. Particle viscosity assessment based on H_{obs}/W aspect ratios of individual particles measured from SEM images taken at an 80° tilted angle. Upper and lower panels show measurements corresponding to the late afternoon samples and nighttime samples, respectively. Panels are arranged left-to-right to reflect increasing plume age and BBA evolution in daytime and nighttime, respectively.

Pa·s) and glassy (>10^{10} Pa·s) particles, with an average H_{obs}/W of 0.75 ± 0.2, as shown in Figure S10. Conversely, the majority (70%) of the nighttime particles exhibited low viscosity, as indicated by their low average aspect ratios (0.3 ± 0.1), with some contribution from semiviscous particles. An exception to the nighttime trend is sample H56, which presents a broader H_{obs}/W distribution extending over the more viscous range. The distinct case of sample H56 may have resulted due to variations in the oxidation state of carbon which was reported to be the lowest during the period where this sample was collected,[35] making particles less susceptible to water uptake during elevated humidity conditions at nighttime. Differences in particle viscosity are principally attributed to higher relative humidity (RH) during nighttime, which causes hygroscopic growth of particles, prompting their liquid-like transformations due to the plasticizing and dissolving effects of water. The differences in RH measured during the late afternoon and nighttime flights are illustrated in Figure S11. Ambient conditions become more humid at night, with average RH values of ∼40−45% in the late afternoon and ∼50−55% at night. It has been shown, that variations of RH between 40% and 55% can potentially reduce viscosity of BBA particles from ∼10^6 to ∼10^4 Pa·s.[76] This change corresponds to a decrease in characteristic *e*-folding diffusion times for 200 nm particles from several hours to just a few minutes.[77] Moreover, formation of highly viscous tar balls during daytime biomass burning events has been previously reported and is often attributed to the loss of water, degassing of intermediate and semivolatile organic components, and the polymerization of remaining organic species induced by sunlight exposure.[19,70,71,78−80] While the H_{obs}/W ratios method offers a semiquantitative approach to distinguish between liquid-like, semiviscous, and glassy BBA,[54] a more quantitative assessment of particle viscosity remains challenging and is beyond the scope of this study.

Chemical Speciation and Internal Mixing of Particles. Chemical speciation of carbon functionality within individual particles was determined from STXM/NEXAFS data sets. The average NEXAFS spectra collected at the carbon K-edge for all selected in-plume samples are shown in Figure S12. The OD profiles from NEXAFS measurements reflect the overlapping absorption bands of various carbon transition energies. To

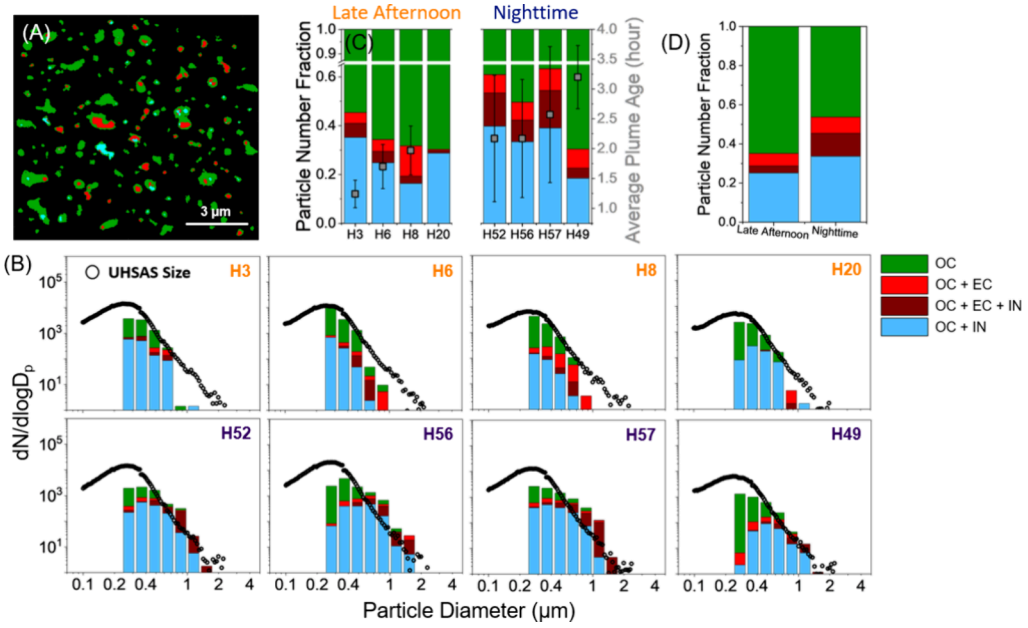

Figure 4. (A) Representative STXM map of BBA particles from sample H57, showing distribution of OC (green), EC (red), and IN (teal). (B) PSDs acquired from STXM chemical imaging compared to UHSAS size measurements; two data sets are superimposed and anchored at 0.50 μm to facilitate visual comparison. Individual panels are arranged left-to-right to reflect increasing plume age and aerosol evolution during late afternoon and nighttime, respectively. (C) Normalized relative contribution of different particle internally mixed classes in individual samples shown in respect to plume age (error bars indicate uncertainty of the plume age calculations). (D) Relative contribution of particle heterogeneity classifications, reported as fractions of total particle count, representative of late afternoon and nighttime smoke plumes.

https://doi.org/10.1021/acsestair.4c00242
ACS EST Air 2025, 2, 508−521

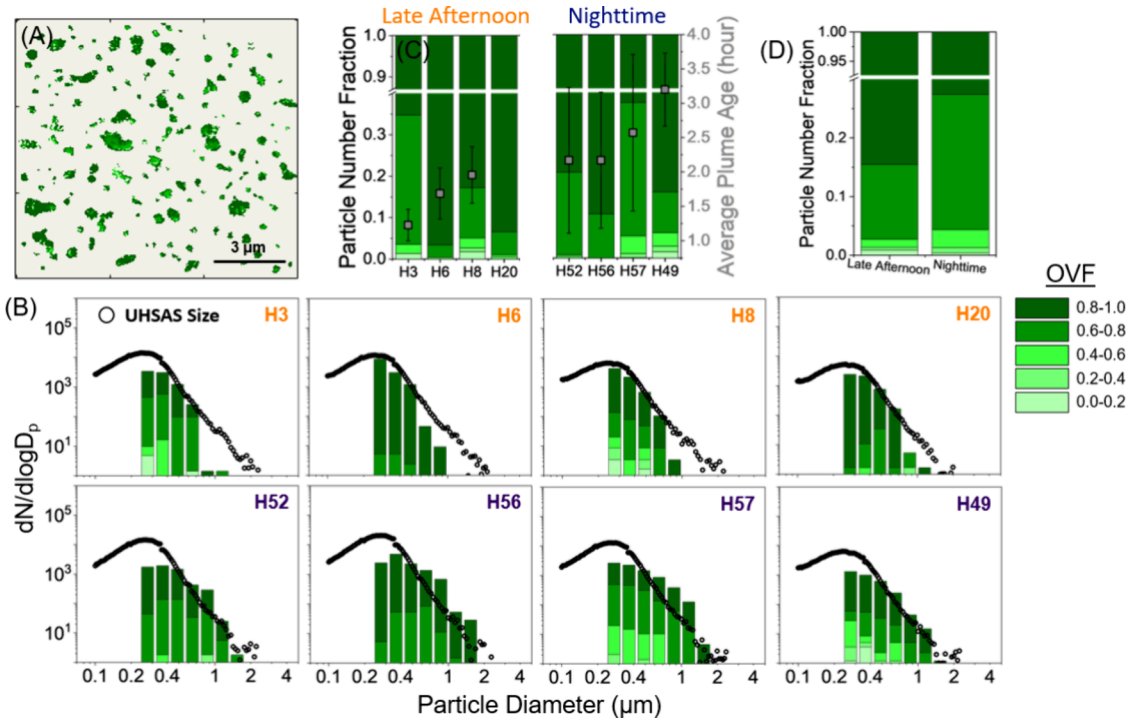

Figure 5. (A) Representative map of spatially resolved, particle-specific OVF measurements. (B) PSDs acquired from chemical imaging compared to UHSAS size measurements; two data sets are superimposed and anchored at 0.50 μm to facilitate visual comparison. Individual panels are arranged left-to-right to reflect increasing plume age and aerosol evolution during late afternoon and nighttime, respectively. (C) Normalized relative contribution of particles with different OVF as a function of plume age (error bars indicate uncertainty of the plume age calculations). (D) Relative contribution of particle OVF ranges, reported as fractions of total particle count, representative of late afternoon and nighttime smoke plumes.

determine carbon speciation and the contribution of each organic group to the total X-ray absorption, the average spectra were deconvoluted. All samples exhibited complex chemical speciation, with contributions from alkene, carboxyl, alcohol, carbonyl, and aliphatic groups, along with traces of carbonate ($-CO_3$), as illustrated in Figures S13 and S14. Despite this chemical diversity, the late afternoon samples showed higher contribution from oxygenated functional groups to the total NEXAFS spectra. Specifically, carboxyl and carbonyl groups accounted for 20% and 19% of the total X-ray absorption, respectively, compared to ∼ 15% in the nighttime samples. Differences between late afternoon and nighttime flights were also evident in the AMS-derived oxidation state of carbon and oxygen-to-carbon ratios.[35] These discrepancies likely result from previously reported differences in the combustion conditions at the time of emission between late afternoon and nighttime smokes,[35] as well as higher sunlight exposure during late afternoon, which promotes the photooxidation of VOCs. Additional peaks were observed at 297.1 and 299.7 eV, which correspond to L3 and L2 edges of potassium,[55] respectively, consistent with the elemental microanalysis results obtained from CCSEM/EDX. STXM measurements were further used to assess chemical heterogeneity within individual particles, distinguishing between their OC, EC, and IN components, and their lateral arrangements within individual particles, which influence the optical and hygroscopic properties of aerosols.[81] A representative carbon "map" shown in Figure 4A illustrates the internal mixing of the three principal chemical components. Similar to results of EDX microanalysis, particles were predominantly composed of organic species, with some EC content and traces of IN. The lateral distribution of OC, EC, and IN was evaluated on a per-pixel basis to categorize components of individual particles as OC, OC+EC, OC+EC+IN, and OC+IN. A detailed description of this particle classification framework using STXM "maps" is provided elsewhere.[55] Figure 4B presents STXM-determined PSDs overlaid with the particle size data for all in-plume samples, along with the internal mixing state classifications for each size bin. The particle number concentrations in the nighttime samples were overestimated for larger particles reported by STXM and CCSEM. This overestimation is attributed to the large contribution of liquid-like particles frequent in the nighttime samples, which resulted in greater flattening upon impaction and, consequently, a larger apparent 2D projected area of the imaged particles. Figure 4C illustrates the internal heterogeneity of individual particles from late afternoon and nighttime samples, showing an overall increase in the fraction of particles entirely comprised of OC, indicative of a buildup of organic components downwind of the emission source. Figure 4D shows that this process is more pronounced during late afternoon, with approximately 65% of the total particle population consisting entirely of OC, compared to around 46% for nighttime particles. Additionally, IN-containing particles (i.e., OC+IN and OC+EC+IN) are more dominant in night samples, contributing to approximately 45% of the analyzed particles. In the late afternoon samples, their fraction is smaller, at 29%, which is consistent with the CCSEM/EDX findings. Particles with all three components (OC+EC+IN) account for a larger fraction in nighttime samples (∼12%) compared to those collected during the late afternoon (∼4%). While all late afternoon and nighttime particles encompass a mixture of OC, EC, and IN, enhanced

https://doi.org/10.1021/acsestair.4c00242
ACS EST Air 2025, 2, 508−521

sunlight exposure during the late afternoon flight favors a more pronounced photochemical accumulation of SOA material during smoke plume transport. Consequently, late afternoon BBA particles are more chemically homogeneous as the buildup of OC effectively masks the contributions of EC and IN particle components.

Organic Volume Fraction and Hygroscopicity Parameters. The OVFs determined from STXM/NEXAFS data are commonly used to investigate the evolution of aerosols emitted from biomass burning events, providing insight into the accumulation or loss of organic and inorganic materials on individual particles.[43] Figure 5A displays a representative map of spatially resolved OVF, calculated using eqs E1−E5 summarized in Supporting Information, Note 4. The field-of-view shown in this figure corresponds to the same region shown in Figure 4A, where the presence of IN and EC is evident in areas with low OVF, confirming the effectiveness of these two types of STXM "maps" in evaluating the organic content within particles. Figure 5B presents size-resolved OVFs for the late afternoon and nighttime particle samples, alongside the UHSAS size data, similar to Figures 2B and 4B. Notably, both late afternoon and nighttime samples are dominated by particles with OVF > 0.6. However, Figure 5C,D reveals that the late afternoon samples contain a larger fraction of particles (~85%) classified as mostly organic (i.e., OVF = 0.8−1.0), compared to the nighttime samples (~73%).

Similar to previous research,[43] the OVFs were employed to evaluate the water uptake activity of collected BBA particles, addressing the uncertain impact of biomass burning smoke plumes on cloud forming properties.[82] Average OVF corresponding to individual late afternoon and nighttime samples are listed in Supporting Information, Note 4. The κ parameter,[59] which characterizes the hygroscopic behavior of aerosols, was calculated on a per-particle basis using eq 2. Figure 6A illustrates the distribution of κ values for each individual plume sample, revealing significant variability. The mean κ values range between 0.20 and 0.32, with the lowest value (~0.21) observed during the late afternoon (i.e., H6 and H20) and the highest value (~0.31) during nighttime (H57). These values are consistent with previously reported κ values for mixed organic/inorganic BBA particles sampled at different times (~0.12−0.25).[43,83] To compare the relative hygroscopicity of BBA from late afternoon and nighttime emissions, κ values from the same flight were combined and averaged. Figure 6B presents representative κ parameters for both flights, calculated to be approximately 0.24 for late afternoon particles and 0.28 for nighttime particles. This suggests that nighttime particles are more hygroscopic and have a higher potential to serve as cloud condensation nuclei (CCN). The temporal variations in water uptake activity can be attributed to differences in ambient RH and the content of water-soluble inorganic species within aerosols, particularly K-containing particles, which were found to have a greater presence in the nighttime samples. It is important to note that STXM-derived κ values are influenced by OVF calculations, which can vary by ~ 10% and ~ 35% depending on the assumed organic and inorganic reference compounds, respectively.[52,56,84] Consequently, this study focuses only on comparing the relative trends in the κ values calculated for the late afternoon and nighttime BBA particles.

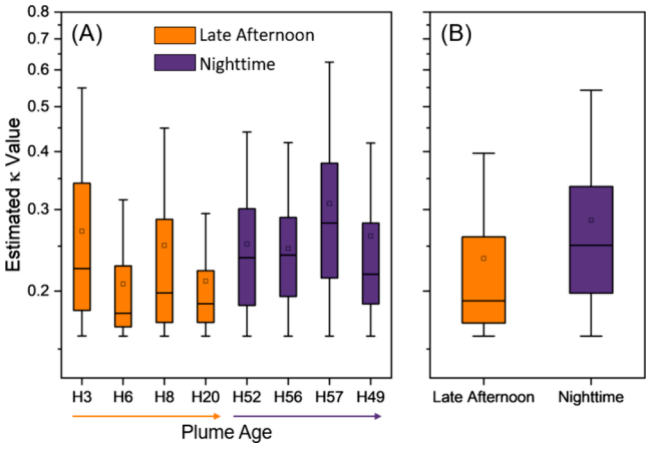

Figure 6. Hygroscopicity parameter κ estimated from STXM-derived OVFs for (A) individual late afternoon and nighttime samples and (B) averaged for the late afternoon and nighttime data sets.

Particle Mixing State and Diversity. The assessment of particle diversity and mixing state metrics utilizes the mass fractions of individual components within each particle, as previously described.[62] In this study, mass fraction metrics were derived from STXM/NEXAFS measurements and calculated using eqs E12−E14 (Supporting Information, Note 5), focusing on three individual components: OC, EC, and IN, as illustrated in Figure S15a,c. Across all samples, OC consistently contributes the largest fraction, while EC is also commonly present. IN fractions are notably more prevalent in particles from the nighttime samples, consistent with CCSEM/EDX findings. Mass fractions were further used to calculate the Shannon entropy (H_i) of component distribution within a particle, from which the particle specific diversity (D_i) is calculated using eq E18. D_i reflects the number of components within individual particles, ranging from 1 (only one component contributes the total particle mass) to a maximum of 3 (equal fractions OC, EC, and IN contribute to an individual particle). Noninteger D_i values indicate uneven contributions from these three components. D_i values computed for particles from the late afternoon and nighttime samples are included in Figure S15b and d, respectively. Nighttime particles exhibit greater chemical diversity, with comparable contributions OC, EC, and IN, whereas late afternoon particles show minimal or no presence of IN. Further mixing state information was inferred from the bulk diversity (D_γ) and average particle diversity (D_α) metrics. D_γ represents the number of components in the particle bulk, while D_α indicates the average number of components within individual particles. Similar to D_i, these diversity parameters yield noninteger values when the mass fractions of OC, EC, and IN are unequal. D_γ and D_α were then used to calculate the mixing state index χ using eq E21, which describes the representativeness of the chemical composition of individual particles compared to the particle population and discriminates between internally and externally mixed particle populations. Figure 7 presents D_γ, D_α, and χ metrics representative of in-plume and background samples collected during both flights. Late afternoon and nighttime samples form distinct groups based on their mixing state parameters, with nighttime BBA particles exhibiting higher chemical diversity, as indicated by elevated D_γ and D_α values. These differences are primarily due to higher IN fractions in the nighttime samples, contributing to a more heterogeneous chemical composition. Despite the variations in D_γ and D_α between late afternoon and nighttime

https://doi.org/10.1021/acsestair.4c00242
ACS EST Air 2025, 2, 508−521

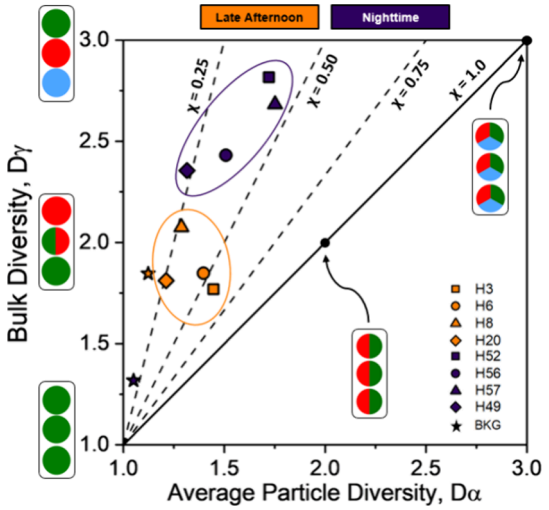

Figure 7. Mixing state diagram for late afternoon and nighttime samples showing bulk (D_γ) and average single particle (D_α) diversity parameters. Dashed lines represent thresholds for mixing state index (χ) values established previously by Riemer and West, 2023. Four cartoon illustrations represent examples of different mixing states.

particles, most samples exhibit χ values below 0.50, indicating that individual particles are externally mixed and not chemically representative of the bulk. In the D_γ vs D_α space, particles from late afternoon samples are more tightly clustered compared to those from the nighttime, indicating greater compositional variability in the nighttime particles. This observation aligns with the slightly broader distributions of their κ values, as shown in Figure 6. The χ values reported in this study are consistent with previous findings, with BBA particles typically showing χ values between 0.25 and 0.50.[43] A more detailed analysis of the expected correlation between plume age and mixing state index χ is beyond the scope of this study, as the plume aging time between adjacent samples is likely too short for significant chemical transformations detectable by spectro-microscopy imaging techniques.

Light-Absorbing Properties of BBA. Light absorption by WSOC was measured across the UV−vis wavelength range (310−500 nm) with a 10 s resolution using the BrC-PILS instrument, as previously documented.[85] These measurements, combined with WSOC concentrations, enabled the calculation of the mass absorption coefficient of BrC components (MAC_{BrC}) within individual samples.[36] The detailed procedures for MAC_{BrC} calculations during the microscopy sampling periods are outlined in Supporting Information, Note 10. As illustrated in Figure S16, both late afternoon and nighttime samples exhibited higher MAC_{BrC} values in the shorter wavelength range (310−330 nm), followed by an exponential decline at longer wavelengths − a typical characteristic of BrC.[86,87] To quantify this wavelength-dependent light absorption, absorption Ångström exponent (AAE) coefficients were calculated and compared between late afternoon and nighttime samples. Specifically, AAE values were derived from the BrC-PILS absorbance records integrated over corresponding time periods for each sample, using linear regression fits of $\ln(MAC_{BrC})$ vs $\ln(\lambda)$ data, as shown in Figure S17. To improve linearity and facilitate comparison between AAE optical values, MAC_{BrC} was reported within the 330−440 nm wavelength range. Generally, the late afternoon samples had higher AAE values than nighttime ones.

An assessment of light absorption properties of BrC from various sources was previously conducted to establish an optical classification framework.[88] While the approach was initially introduced using the imaginary part of the particle refractive index at wavelength 550 nm and the power law exponent, our study categorizes samples based on the correlation between AAE and $\log_{10}$ MAC_{BrC_400nm}, leveraging the reliability of MAC_{BrC} measurements at shorter wavelengths. Conversions between the optical parameters initially utilized and those reported in this study are described elsewhere.[80] Figure 8 presents the AAE vs $\log_{10}$ MAC_{BrC_400nm}

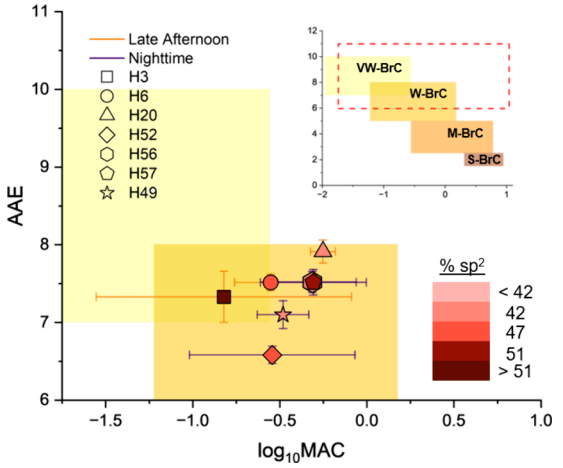

Figure 8. Optical classification of BBA following the framework of Saleh.[88] Filled rectangles in the top right corner diagram highlight BrC ranges of very weakly (VW), weakly (W), moderately (M), and strongly (S) absorbing BrC. Dashed rectangle illustrates region of AAE and $\log_{10}$ MAC values shown in the main figure. Error bars on the *x*-axis represent the standard deviation of the $\log_{10}$ MAC_{400nm} values. Error bars on the *y*-axis represent the uncertainties of the slopes (*AAE*) as calculated from the linear fits. Orange and dark purple error bars correspond to late afternoon and nighttime samples, respectively. Data points are color-coded with respect to the STXM-derived % sp^2 hybridization metric.

data from our study, mapped with respect to four optical classes: very weakly (VW-), weakly (W-), moderately (M-), and strongly (S-) absorbing BrC. The optical properties of BBA from WSOC-BrC measurements for all late afternoon and nighttime samples predominantly fall within the W-BrC class, with $\log_{10}$ MAC_{BrC_400nm} values extending into the M-BrC range if AAE values are not considered. These findings align with previous studies investigating BBA particles.[80,89,90]

Given that BrC optical properties of particles are inherently related to the extent of π-bond conjugation in their organic components,[21] values of % sp2 (C*═C) hybridization were derived from NEXAFS spectra of individual particles in each of the microscopy samples collected (color legend in Figure 8). Detailed derivation of this metric is shown in Supporting Information, Note 11. Both graphitic (elemental) and aromatic carbon have high percentages of sp^2 hybridization. The average % sp^2 hybridization falls within the range of 40−60% across all samples, consistent with previously reported values for BBA particles.[21] A loose inverse correlation exists between calculated AAE from the WSOC-BrC measurements and % sp^2 hybridization calculated from the NEXAFS spectra that is more pronounced in the late afternoon flight. Thus, the wavelength dependency of light absorption by the water-

https://doi.org/10.1021/acsestair.4c00242
ACS EST Air 2025, 2, 508−521

soluble components of BBA particles and the extent of contributions from compounds with π-bonding and sp^2 hybrid orbitals in the microscopy samples indicate complementary characteristics of BBA optical properties and composition. It is important to recognize the limitations of this analysis in establishing a direct empirical correlation between the chemical and optical properties of collected samples. Highly oriented graphitic or aromatic material (high % sp^2 hybridization) with relatively high absorption properties remains undetected by the BrC-PILS instrument due to its insolubility in water, leading to negative biases in BrC-PILS measurements of BrC content and its light absorption. Therefore, the results shown in Figure 8 should be interpreted with caution as these likely reflect an upper limit of AAE values and possibly a lower limit of MAC values for BrC from ambient BBA.

CONCLUSIONS

This study examined variations in chemical composition and optical properties of particles emitted from the same wildfire during the late afternoon and at night. Using complementary spectromicroscopy techniques, we performed detailed chemical imaging of individual particles. No consistent trend in composition and mixing states was observed at different plume ages within one flight, suggesting that particle aging processes may not have been sufficiently explored with the experimental time scales for the CCSEM/EDX analysis. However, distinct differences were noted between late afternoon and nighttime BBA particles. While organic components dominated all samples, nighttime particles showed greater chemical complexity with higher contributions from inorganic species, particularly potassium salts. This was reflected in their lower OVF values and increased chemical diversity. The accumulation of secondary organic material due to photochemical processes led to a higher fraction of organic carbon particles in the STXM spectra of late afternoon samples. Viscosity assessments using electron microscopy images indicated that nighttime BBA particles, influenced by higher relative humidity and inorganic salts, exhibited more liquid-like viscosity potentially suggesting faster dissolution and mixing of soluble components. Online BrC-PILS measurements of light absorption enabled calculations of MAC_{400nm} and AAE values, categorizing the samples as "weakly" to "moderately absorbing" BrC. The % sp^2 hybridization from STXM/NEXAFS spectra, ranging between 40 and 60%, indicated a mixture of EC and OC components, with a loose inverse correlation between AAE and % sp^2 hybridization.

This study's multimodal approach offers valuable insights into the chemical, viscoelastic, hygroscopic, and optical properties of BBA particles, showing significant differences between late afternoon and nighttime BBA particles, influenced by factors like the burn conditions at the time of emission, sunlight exposure, and relative humidity. These diurnal differences suggest that the environmental impact of BBA emitted from the same source could vary depending on the time of day, with nighttime particles potentially being more effective at promoting cloud formation due to their higher hygroscopicity. These findings highlight the need for more comprehensive assessments of individual particles and their transformations, underscoring the importance of considering their complex metrics and properties in modeling predictions of BBA impacts on the atmosphere.

ASSOCIATED CONTENT

Supporting Information

The Supporting Information is available free of charge at https://pubs.acs.org/doi/10.1021/acsestair.4c00242.

3D flight maps; Plume age calculations; CCSEM/EDX and STXM/NEXAFS statistics; Description of STXM/NEXAFS measurements; Description of OVF metrics; Mass fractions and mixing state parametrization; *k*-means clustering; Particle viscosity assessment from SEM images; NEXAFS carbon spectra deconvolution; Real-time optical metrics; STXM-derived % sp^2 hybridization values (PDF)

AUTHOR INFORMATION

Corresponding Author

Alexander Laskin − *Department of Chemistry and Department of Earth, Atmospheric and Planetary Sciences, Purdue University, West Lafayette, Indiana 47907, United States;* orcid.org/0000-0002-7836-8417; Email: alaskin@purdue.edu

Authors

Felipe A. Rivera-Adorno − *Department of Chemistry, Purdue University, West Lafayette, Indiana 47907, United States;* orcid.org/0000-0002-7355-7999

Jay M. Tomlin − *Department of Chemistry, Purdue University, West Lafayette, Indiana 47907, United States;* Present Address: Atmospheric Science Branch, NASA Ames Research Center, Moffett Field, CA 94035, U.S.A; orcid.org/0000-0002-3081-1512

Nurun Nahar Lata − *Environmental Molecular Sciences Laboratory, Pacific Northwest National Laboratory, Richland, Washington 99352, United States;* orcid.org/0000-0003-1466-3545

Lisa Azzarello − *Department of Chemistry, York University, Toronto, Ontario M3J 1P3, Canada;* orcid.org/0000-0002-5348-1595

Michael A. Robinson − *Chemical Sciences Laboratory, National Oceanic and Atmospheric Administration, Boulder, Colorado 80305, United States; Cooperative Institute for Research in Environmental Sciences, University of Colorado, Boulder, Colorado 80309, United States*

Rebecca A. Washenfelder − *Chemical Sciences Laboratory, National Oceanic and Atmospheric Administration, Boulder, Colorado 80305, United States;* orcid.org/0000-0002-8106-3702

Alessandro Franchin − *Atmospheric Chemistry Observations and Modelling Laboratory, University Corporation for Atmospheric Research, Boulder, Colorado 80307, United States*

Ann M. Middlebrook − *Chemical Sciences Laboratory, National Oceanic and Atmospheric Administration, Boulder, Colorado 80305, United States;* orcid.org/0000-0002-2984-6304

Swarup China − *Environmental Molecular Sciences Laboratory, Pacific Northwest National Laboratory, Richland, Washington 99352, United States;* orcid.org/0000-0001-7670-335X

Steven S. Brown − *Chemical Sciences Laboratory, National Oceanic and Atmospheric Administration, Boulder, Colorado 80305, United States; Department of Chemistry, University*

of Colorado, Boulder, Colorado 80309, United States; orcid.org/0000-0001-7477-9078

Cora J. Young − *Department of Chemistry, York University, Toronto, Ontario M3J 1P3, Canada;* orcid.org/0000-0002-6908-5829

Matthew Fraund − *Fraund Consulting, Pleasant Hill, California 94523, United States;* orcid.org/0000-0002-7460-4283

Ryan C. Moffet − *Sonoma Technology, Inc., Petaluma, California 94954, United States;* orcid.org/0000-0002-2352-5454

Complete contact information is available at: https://pubs.acs.org/10.1021/acsestair.4c00242

Author Contributions

F.R. and A.L. devised the project. R.W., A.M., S.B., L.A., M.R., and A.F. worked on the acquisition and processing of online chemical, optical, and size data. F.R., J.T., N.N.L, and S.C. conducted SEM and CCSEM/EDX measurements. F.R., J.T., M. F., and R.M. conducted STXM/NEXAFS measurements. F.R analyzed and integrated all data sets. F.R. and A.L. wrote the manuscript with contributions from all coauthors.

Notes

The authors declare no competing financial interest.

■ ACKNOWLEDGMENTS

This work of the Purdue and STI groups was supported by the U.S. Department of Energy's (DOE) Atmospheric System Research Program, Office of Biological and Environmental Research (OBER), Award DE-SC0021977. We thank all the members of the NOAA Twin Otter group for assisting during the sample collection process onboard the research aircraft and to those who worked on online data acquisition and processing. The authors would like to acknowledge Gregory Eakins from the Jonathan Amy Facility for Chemical Instrumentation (JAFCI) at Purdue University for preparing the aerosol collector deployed in this study. The CCSEM/EDX imaging for this project was performed at the Environmental Molecular Sciences Laboratory at Pacific Northwest National Laboratory. We would like to acknowledge Beamline 5.3.2.2 of the Advanced Light Source at Lawrence Berkeley National Laboratory and the Beamline scientist Matthew Marcus for his guidance when operating STXM/XEFAS. Additional SEM imaging was performed at the Life Sciences Microscope Facility at Purdue University for particle viscosity assessment.

■ REFERENCES

(1) Richardson, D.; Black, A. S.; Irving, D.; Matear, R. J.; Monselesan, D. P.; Risbey, J. S.; Squire, D. T.; Tozer, C. R. Global Increase in Wildfire Potential from Compound Fire Weather and Drought. *npj Clim. Atmos. Sci.* **2022**, *5* (1), 23.

(2) Bluvshtein, N.; Lin, P.; Flores, J. M.; Segev, L.; Mazar, Y.; Tas, E.; Snider, G.; Weagle, C.; Brown, S. S.; Laskin, A.; Rudich, Y. Broadband Optical Properties of Biomass-burning Aerosol and Identification of Brown Carbon Chromophores. *JGR Atmospheres* **2017**, *122* (10), 5441−5456.

(3) Ponczek, M.; Franco, M. A.; Carbone, S.; Rizzo, L. V.; Monteiro Dos Santos, D.; Morais, F. G.; Duarte, A.; Barbosa, H. M. J.; Artaxo, P. Linking the Chemical Composition and Optical Properties of Biomass Burning Aerosols in Amazonia. *Environ. Sci.: Atmos.* **2022**, *2* (2), 252−269.

(4) Spracklen, D. V.; Carslaw, K. S.; Pöschl, U.; Rap, A.; Forster, P. M. Global Cloud Condensation Nuclei Influenced by Carbonaceous Combustion Aerosol. *Atmos. Chem. Phys.* **2011**, *11* (17), 9067−9087.

(5) Liu, L.; Cheng, Y.; Wang, S.; Wei, C.; Pöhlker, M. L.; Pöhlker, C.; Artaxo, P.; Shrivastava, M.; Andreae, M. O.; Pöschl, U.; Su, H. Impact of Biomass Burning Aerosols on Radiation, Clouds, and Precipitation over the Amazon: Relative Importance of Aerosol-Cloud and Aerosol-Radiation Interactions. *Atmos. Chem. Phys.* **2020**, *20* (21), 13283−13301.

(6) Kaulfus, A. S.; Nair, U.; Jaffe, D.; Christopher, S. A.; Goodrick, S. Biomass Burning Smoke Climatology of the United States: Implications for Particulate Matter Air Quality. *Environ. Sci. Technol.* **2017**, *51* (20), 11731−11741.

(7) Lin, N.-H.; Tsay, S.-C.; Maring, H. B.; Yen, M.-C.; Sheu, G.-R.; Wang, S.-H.; Chi, K. H.; Chuang, M.-T.; Ou-Yang, C.-F.; Fu, J. S.; Reid, J. S.; Lee, C.-T.; Wang, L.-C.; Wang, J.-L.; Hsu, C. N.; Sayer, A. M.; Holben, B. N.; Chu, Y.-C.; Nguyen, X. A.; Sopajaree, K.; Chen, S.-J.; Cheng, M.-T.; Tsuang, B.-J.; Tsai, C.-J.; Peng, C.-M.; Schnell, R. C.; Conway, T.; Chang, C.-T.; Lin, K.-S.; Tsai, Y. I.; Lee, W.-J.; Chang, S.-C.; Liu, J.-J.; Chiang, W.-L.; Huang, S.-J.; Lin, T.-H.; Liu, G.-R. An Overview of Regional Experiments on Biomass Burning Aerosols and Related Pollutants in Southeast Asia: From BASE-ASIA and the Dongsha Experiment to 7-SEAS. *Atmos. Environ.* **2013**, *78*, 1−19.

(8) McClure, C. D.; Jaffe, D. A. US Particulate Matter Air Quality Improves except in Wildfire-Prone Areas. *Proc. Natl. Acad. Sci. U.S.A.* **2018**, *115* (31), 7901−7906.

(9) Chen, J.; Li, C.; Ristovski, Z.; Milic, A.; Gu, Y.; Islam, M. S.; Wang, S.; Hao, J.; Zhang, H.; He, C.; Guo, H.; Fu, H.; Miljevic, B.; Morawska, L.; Thai, P.; Lam, Y. F.; Pereira, G.; Ding, A.; Huang, X.; Dumka, U. C. A Review of Biomass Burning: Emissions and Impacts on Air Quality, Health and Climate in China. *Sci. Total Environ.* **2017**, *579*, 1000−1034.

(10) de Oliveira Alves, N.; Brito, J.; Caumo, S.; Arana, A.; de Souza Hacon, S.; Artaxo, P.; Hillamo, R.; Teinilä, K.; Batistuzzo de Medeiros, S. R.; de Castro Vasconcellos, P. Biomass Burning in the Amazon Region: Aerosol Source Apportionment and Associated Health Risk Assessment. *Atmos. Environ.* **2015**, *120*, 277−285.

(11) Rappold, A. G.; Stone, S. L.; Cascio, W. E.; Neas, L. M.; Kilaru, V. J.; Carraway, M. S.; Szykman, J. J.; Ising, A.; Cleve, W. E.; Meredith, J. T.; Vaughan-Batten, H.; Deyneka, L.; Devlin, R. B. Peat Bog Wildfire Smoke Exposure in Rural North Carolina Is Associated with Cardiopulmonary Emergency Department Visits Assessed through Syndromic Surveillance. *Environ. Health Perspect.* **2011**, *119* (10), 1415−1420.

(12) Thelen, B.; French, N. H.; Koziol, B. W.; Billmire, M.; Owen, R. C.; Johnson, J.; Ginsberg, M.; Loboda, T.; Wu, S. Modeling Acute Respiratory Illness during the 2007 San Diego Wildland Fires Using a Coupled Emissions-Transport System and Generalized Additive Modeling. *Environ. Health* **2013**, *12* (1), 94.

(13) Ahern, A. T.; Robinson, E. S.; Tkacik, D. S.; Saleh, R.; Hatch, L. E.; Barsanti, K. C.; Stockwell, C. E.; Yokelson, R. J.; Presto, A. A.; Robinson, A. L.; Sullivan, R. C.; Donahue, N. M. Production of Secondary Organic Aerosol During Aging of Biomass Burning Smoke From Fresh Fuels and Its Relationship to VOC Precursors. *JGR Atmospheres* **2019**, *124* (6), 3583−3606.

(14) Theodoritsi, G. N.; Pandis, S. N. Simulation of the Chemical Evolution of Biomass Burning Organic Aerosol. *Atmos. Chem. Phys.* **2019**, *19* (8), 5403−5415.

(15) Akherati, A.; He, Y.; Coggon, M. M.; Koss, A. R.; Hodshire, A. L.; Sekimoto, K.; Warneke, C.; De Gouw, J.; Yee, L.; Seinfeld, J. H.; Onasch, T. B.; Herndon, S. C.; Knighton, W. B.; Cappa, C. D.; Kleeman, M. J.; Lim, C. Y.; Kroll, J. H.; Pierce, J. R.; Jathar, S. H. Oxygenated Aromatic Compounds Are Important Precursors of Secondary Organic Aerosol in Biomass-Burning Emissions. *Environ. Sci. Technol.* **2020**, *54* (14), 8568−8579.

(16) Reid, J. S.; Koppmann, R.; Eck, T. F.; Eleuterio, D. P. A Review of Biomass Burning Emissions Part II: Intensive Physical Properties of Biomass Burning Particles. *Atmos. Chem. Phys.* **2005**, *5*, 799−825.

(17) Kondo, Y.; Matsui, H.; Moteki, N.; Sahu, L.; Takegawa, N.; Kajino, M.; Zhao, Y.; Cubison, M. J.; Jimenez, J. L.; Vay, S.; Diskin, G. S.; Anderson, B.; Wisthaler, A.; Mikoviny, T.; Fuelberg, H. E.; Blake, D. R.; Huey, G.; Weinheimer, A. J.; Knapp, D. J.; Brune, W. H. Emissions of Black Carbon, Organic, and Inorganic Aerosols from Biomass Burning in North America and Asia in 2008. *J. Geophys. Res.* **2011**, *116* (D8), D08204.
(18) Pratt, K. A.; Murphy, S. M.; Subramanian, R.; DeMott, P. J.; Kok, G. L.; Campos, T.; Rogers, D. C.; Prenni, A. J.; Heymsfield, A. J.; Seinfeld, J. H.; Prather, K. A. Flight-Based Chemical Characterization of Biomass Burning Aerosols within Two Prescribed Burn Smoke Plumes. *Atmos. Chem. Phys.* **2011**, *11* (24), 12549−12565.
(19) Adachi, K.; Sedlacek, A. J.; Kleinman, L.; Springston, S. R.; Wang, J.; Chand, D.; Hubbe, J. M.; Shilling, J. E.; Onasch, T. B.; Kinase, T.; Sakata, K.; Takahashi, Y.; Buseck, P. R. Spherical Tarball Particles Form through Rapid Chemical and Physical Changes of Organic Matter in Biomass-Burning Smoke. *Proc. Natl. Acad. Sci. U.S.A.* **2019**, *116* (39), 19336−19341.
(20) Kong, X.; Priestley, M.; Pei, X.; Zhu, Y.; Wu, Z.; Hu, M.; Ohigashi, T.; Yuzawa, H.; Pathak, R. K.; Pettersson, J. B. C.; Hallquist, M. Chemical Mapping of Potassium-Containing Particles from Residential Biomass Burning and in Ambient Air. *AIP Conf. Proc.* **2023**, *2990*, 020003.
(21) Hopkins, R. J.; Lewis, K.; Desyaterik, Y.; Wang, Z.; Tivanski, A. V.; Arnott, W. P.; Laskin, A.; Gilles, M. K. Correlations between Optical, Chemical and Physical Properties of Biomass Burn Aerosols. *Geophys. Res. Lett.* **2007**, *34* (18), L18806.
(22) Collier, S.; Zhou, S.; Onasch, T. B.; Jaffe, D. A.; Kleinman, L.; Sedlacek, A. J.; Briggs, N. L.; Hee, J.; Fortner, E.; Shilling, J. E.; Worsnop, D.; Yokelson, R. J.; Parworth, C.; Ge, X.; Xu, J.; Butterfield, Z.; Chand, D.; Dubey, M. K.; Pekour, M. S.; Springston, S.; Zhang, Q. Regional Influence of Aerosol Emissions from Wildfires Driven by Combustion Efficiency: Insights from the BBOP Campaign. *Environ. Sci. Technol.* **2016**, *50* (16), 8613−8622.
(23) Pandey, A.; Shetty, N. J.; Chakrabarty, R. K. Aerosol Light Absorption from Optical Measurements of PTFE Membrane Filter Samples: Sensitivity Analysis of Optical Depth Measures. *Atmos. Meas. Technol.* **2019**, *12* (2), 1365−1373.
(24) Shi, S.; Cheng, T.; Gu, X.; Guo, H.; Wu, Y.; Wang, Y. Biomass Burning Aerosol Characteristics for Different Vegetation Types in Different Aging Periods. *Environ. Int.* **2019**, *126*, 504−511.
(25) Pokhrel, R. P.; Gordon, J.; Fiddler, M. N.; Bililign, S. Impact of Combustion Conditions on Physical and Morphological Properties of Biomass Burning Aerosol. *Aerosol Sci. Technol.* **2021**, *55* (1), 80−91.
(26) Li, C.; Ma, Z.; Chen, J.; Wang, X.; Ye, X.; Wang, L.; Yang, X.; Kan, H.; Donaldson, D. J.; Mellouki, A. Evolution of Biomass Burning Smoke Particles in the Dark. *Atmos. Environ.* **2015**, *120*, 244−252.
(27) Decker, Z. C. J.; Zarzana, K. J.; Coggon, M.; Min, K.-E.; Pollack, I.; Ryerson, T. B.; Peischl, J.; Edwards, P.; Dubé, W. P.; Markovic, M. Z.; Roberts, J. M.; Veres, P. R.; Graus, M.; Warneke, C.; de Gouw, J.; Hatch, L. E.; Barsanti, K. C.; Brown, S. S. Nighttime Chemical Transformation in Biomass Burning Plumes: A Box Model Analysis Initialized with Aircraft Observations. *Environ. Sci. Technol.* **2019**, *53* (5), 2529−2538.
(28) Decker, Z. C. J.; Robinson, M. A.; Barsanti, K. C.; Bourgeois, I.; Coggon, M. M.; DiGangi, J. P.; Diskin, G. S.; Flocke, F. M.; Franchin, A.; Fredrickson, C. D.; Gkatzelis, G. I.; Hall, S. R.; Halliday, H.; Holmes, C. D.; Huey, L. G.; Lee, Y. R.; Lindaas, J.; Middlebrook, A. M.; Montzka, D. D.; Moore, R.; Neuman, J. A.; Nowak, J. B.; Palm, B. B.; Peischl, J.; Piel, F.; Rickly, P. S.; Rollins, A. W.; Ryerson, T. B.; Schwantes, R. H.; Sekimoto, K.; Thornhill, L.; Thornton, J. A.; Tyndall, G. S.; Ullmann, K.; Van Rooy, P.; Veres, P. R.; Warneke, C.; Washenfelder, R. A.; Weinheimer, A. J.; Wiggins, E.; Winstead, E.; Wisthaler, A.; Womack, C.; Brown, S. S. Nighttime and Daytime Dark Oxidation Chemistry in Wildfire Plumes: An Observation and Model Analysis of FIREX-AQ Aircraft Data. *Atmos. Chem. Phys.* **2021**, *21* (21), 16293−16317.
(29) June, N. A.; Hodshire, A. L.; Wiggins, E. B.; Winstead, E. L.; Robinson, C. E.; Thornhill, K. L.; Sanchez, K. J.; Moore, R. H.; Pagonis, D.; Guo, H.; Campuzano-Jost, P.; Jimenez, J. L.; Coggon, M. M.; Dean-Day, J. M.; Bui, T. P.; Peischl, J.; Yokelson, R. J.; Alvarado, M. J.; Kreidenweis, S. M.; Jathar, S. H.; Pierce, J. R. Aerosol Size Distribution Changes in FIREX-AQ Biomass Burning Plumes: The Impact of Plume Concentration on Coagulation and OA Condensation/Evaporation. *Atmos. Chem. Phys.* **2022**, *22* (19), 12803−12825.
(30) Brodrick, P. G.; Thompson, D. R.; Garay, M. J.; Giles, D. M.; Holben, B. N.; Kalashnikova, O. V. Simultaneous Characterization of Wildfire Smoke and Surface Properties With Imaging Spectroscopy During the FIREX-AQ Field Campaign. *JGR Atmospheres* **2022**, *127* (7), No. e2021JD034905.
(31) Howell, S. G.; Freitag, S.; Dobracki, A.; Smirnow, N.; Sedlacek, A. J., III Undersizing of Aged African Biomass Burning Aerosol by an Ultra-High-Sensitivity Aerosol Spectrometer. *Atmos. Meas. Technol.* **2021**, *14* (11), 7381−7404.
(32) Zhang, Q.; Jimenez, J. L.; Canagaratna, M. R.; Ulbrich, I. M.; Ng, N. L.; Worsnop, D. R.; Sun, Y. Understanding Atmospheric Organic Aerosols via Factor Analysis of Aerosol Mass Spectrometry: A Review. *Anal. Bioanal. Chem.* **2011**, *401* (10), 3045−3067.
(33) Fortenberry, C. F.; Walker, M. J.; Zhang, Y.; Mitroo, D.; Brune, W. H.; Williams, B. J. Bulk and Molecular-Level Characterization of Laboratory-Aged Biomass Burning Organic Aerosol from Oak Leaf and Heartwood Fuels. *Atmos. Chem. Phys.* **2018**, *18* (3), 2199−2224.
(34) Zhang, X.; Xu, J.; Kang, S.; Liu, Y.; Zhang, Q. Chemical Characterization of Long-Range Transport Biomass Burning Emissions to the Himalayas: Insights from High-Resolution Aerosol Mass Spectrometry. *Atmos. Chem. Phys.* **2018**, *18* (7), 4617−4638.
(35) Rivera-Adorno, F. A.; Azzarello, L.; Robinson, M. A.; Decker, Z. C. J.; Washenfelder, R. A.; Hayden, K.; Franchin, A.; Holmes, C. D.; Young, C. J.; Fredrickson, C. D.; Palm, B.; Schmidt, C.; Soja, A.; Gargulinski, E.; Brown, S. S.; Middlebrook, A. M.; Laskin, A. Aircraft Measurements from a U. S. Western Wildfire Demonstrating Day and Night Differences in Chemical Composition and Optical Properties of Biomass Burning Aerosol and Their Evolution with Age. *ACS Earth Space Chem.* **2025**, *9*, 64.
(36) Washenfelder, R. A.; Azzarello, L.; Ball, K.; Brown, S. S.; Decker, Z. C. J.; Franchin, A.; Fredrickson, C. D.; Hayden, K.; Holmes, C. D.; Middlebrook, A. M.; Palm, B. B.; Pierce, R. B.; Price, D. J.; Roberts, J. M.; Robinson, M. A.; Thornton, J. A.; Womack, C. C.; Young, C. J. Complexity in the Evolution, Composition, and Spectroscopy of Brown Carbon in Aircraft Measurements of Wildfire Plumes. *Geophys. Res. Lett.* **2022**, *49* (9), No. e2022GL098951.
(37) Azzarello, L.; Washenfelder, R. A.; Robinson, M. A.; Franchin, A.; Womack, C. C.; Holmes, C. D.; Brown, S. S.; Middlebrook, A.; Newberger, T.; Sweeney, C.; Young, C. J. Characterization of Water-Soluble Brown Carbon Chromophores from Wildfire Plumes in the Western USA Using Size-Exclusion Chromatography. *Atmos. Chem. Phys.* **2023**, *23* (24), 15643−15654.
(38) Laskin, A.; Moffet, R. C.; Gilles, M. K. Chemical Imaging of Atmospheric Particles. *Acc. Chem. Res.* **2019**, *52* (12), 3419−3431.
(39) Li, W.; Shao, L.; Zhang, D.; Ro, C.-U.; Hu, M.; Bi, X.; Geng, H.; Matsuki, A.; Niu, H.; Chen, J. A Review of Single Aerosol Particle Studies in the Atmosphere of East Asia: Morphology, Mixing State, Source, and Heterogeneous Reactions. *J. Clean. Prod.* **2016**, *112*, 1330−1349.
(40) Jahn, L. G.; Jahl, L. G.; Bland, G. D.; Bowers, B. B.; Monroe, L. W.; Sullivan, R. C. Metallic and Crustal Elements in Biomass-Burning Aerosol and Ash: Prevalence, Significance, and Similarity to Soil Particles. *ACS Earth Space Chem.* **2021**, *5* (1), 136−148.
(41) Jahn, L. G.; Jahl, L. G.; Bowers, B. B.; Sullivan, R. C. Morphology of Organic Carbon Coatings on Biomass-Burning Particles and Their Role in Reactive Gas Uptake. *ACS Earth Space Chem.* **2021**, *5* (9), 2184−2195.
(42) Fraund, M.; Bonanno, D. J.; China, S.; Pham, D. Q.; Veghte, D.; Weis, J.; Kulkarni, G.; Teske, K.; Gilles, M. K.; Laskin, A.; Moffet, R. C. Optical Properties and Composition of Viscous Organic Particles Found in the Southern Great Plains. *Atmos. Chem. Phys.* **2020**, *20* (19), 11593−11606.

https://doi.org/10.1021/acsestair.4c00242
ACS EST Air 2025, 2, 508−521

(43) Tomlin, J. M.; Weis, J.; Veghte, D. P.; China, S.; Fraund, M.; He, Q.; Reicher, N.; Li, C.; Jankowski, K. A.; Rivera-Adorno, F. A.; Morales, A. C.; Rudich, Y.; Moffet, R. C.; Gilles, M. K.; Laskin, A. Chemical Composition and Morphological Analysis of Atmospheric Particles from an Intensive Bonfire Burning Festival. *Environ. Sci.: Atmos.* **2022**, *2* (4), 616−633.
(44) Hopkins, R. J.; Tivanski, A. V.; Marten, B. D.; Gilles, M. K. Chemical Bonding and Structure of Black Carbon Reference Materials and Individual Carbonaceous Atmospheric Aerosols. *J. Aerosol Sci.* **2007**, *38* (6), 573−591.
(45) Bondy, A. L.; Bonanno, D.; Moffet, R. C.; Wang, B.; Laskin, A.; Ault, A. P. The Diverse Chemical Mixing State of Aerosol Particles in the Southeastern United States. *Atmos. Chem. Phys.* **2018**, *18* (16), 12595−12612.
(46) Fraund, M.; Pham, D. Q.; Bonanno, D.; Harder, T. H.; Wang, B.; Brito, J.; De Sá, S. S.; Carbone, S.; China, S.; Artaxo, P.; Martin, S. T.; Pöhlker, C.; Andreae, M. O.; Laskin, A.; Gilles, M. K.; Moffet, R. C. Elemental Mixing State of Aerosol Particles Collected in Central Amazonia during GoAmazon2014/15. *Atmosphere* **2017**, *8* (9), 173.
(47) Warneke, C.; Schwarz, J. P.; Dibb, J.; Kalashnikova, O.; Frost, G.; Al-Saad, J.; Brown, S. S.; Brewer, W. A.; Soja, A.; Seidel, F. C.; Washenfelder, R. A.; Wiggins, E. B.; Moore, R. H.; Anderson, B. E.; Jordan, C.; Yacovitch, T. I.; Herndon, S. C.; Liu, S.; Kuwayama, T.; Jaffe, D.; Johnston, N.; Selimovic, V.; Yokelson, R.; Giles, D. M.; Holben, B. N.; Goloub, P.; Popovici, I.; Trainer, M.; Kumar, A.; Pierce, R. B.; Fahey, D.; Roberts, J.; Gargulinski, E. M.; Peterson, D. A.; Ye, X.; Thapa, L. H.; Saide, P. E.; Fite, C. H.; Holmes, C. D.; Wang, S.; Coggon, M. M.; Decker, Z. C. J.; Stockwell, C. E.; Xu, L.; Gkatzelis, G.; Aikin, K.; Lefer, B.; Kaspari, J.; Griffin, D.; Zeng, L.; Weber, R.; Hastings, M.; Chai, J.; Wolfe, G. M.; Hanisco, T. F.; Liao, J.; Campuzano Jost, P.; Guo, H.; Jimenez, J. L.; Crawford, J. Fire Influence on Regional to Global Environments and Air Quality (FIREX-AQ). *JGR Atmospheres* **2023**, *128* (2), No. e2022JD037758.
(48) Moore, R. H.; Wiggins, E. B.; Ahern, A. T.; Zimmerman, S.; Montgomery, L.; Campuzano Jost, P.; Robinson, C. E.; Ziemba, L. D.; Winstead, E. L.; Anderson, B. E.; Brock, C. A.; Brown, M. D.; Chen, G.; Crosbie, E. C.; Guo, H.; Jimenez, J. L.; Jordan, C. E.; Lyu, M.; Nault, B. A.; Rothfuss, N. E.; Sanchez, K. J.; Schueneman, M.; Shingler, T. J.; Shook, M. A.; Thornhill, K. L.; Wagner, N. L.; Wang, J. Sizing Response of the Ultra-High Sensitivity Aerosol Spectrometer (UHSAS) and Laser Aerosol Spectrometer (LAS) to Changes in Submicron Aerosol Composition and Refractive Index. *Atmos. Meas. Technol.* **2021**, *14* (6), 4517−4542.
(49) Laskin, A.; Iedema, M. J.; Cowin, J. P. Time-Resolved Aerosol Collector for CCSEM/EDX Single-Particle Analysis. *Aerosol Sci. Technol.* **2003**, *37* (3), 246−260.
(50) Laskin, A.; Cowin, J. P.; Iedema, M. J. Analysis of Individual Environmental Particles Using Modern Methods of Electron Microscopy and X-Ray Microanalysis. *J. Electron Spectrosc. Relat. Phenom.* **2006**, *150* (2−3), 260−274.
(51) Ault, A. P.; Peters, T. M.; Sawvel, E. J.; Casuccio, G. S.; Willis, R. D.; Norris, G. A.; Grassian, V. H. Single-Particle SEM-EDX Analysis of Iron-Containing Coarse Particulate Matter in an Urban Environment: Sources and Distribution of Iron within Cleveland, Ohio. *Environ. Sci. Technol.* **2012**, *46* (8), 4331−4339.
(52) Tomlin, J. M.; Jankowski, K. A.; Veghte, D. P.; China, S.; Wang, P.; Fraund, M.; Weis, J.; Zheng, G.; Wang, Y.; Rivera-Adorno, F.; Raveh-Rubin, S.; Knopf, D. A.; Wang, J.; Gilles, M. K.; Moffet, R. C.; Laskin, A. Impact of Dry Intrusion Events on the Composition and Mixing State of Particles during the Winter Aerosol and Cloud Experiment in the Eastern North Atlantic (ACE-ENA). *Atmos. Chem. Phys.* **2021**, *21* (24), 18123−18146.
(53) Tomlin, J. M.; Jankowski, K. A.; Rivera-Adorno, F. A.; Fraund, M.; China, S.; Stirm, B. H.; Kaeser, R.; Eakins, G. S.; Moffet, R. C.; Shepson, P. B.; Laskin, A. Chemical Imaging of Fine Mode Atmospheric Particles Collected from a Research Aircraft over Agricultural Fields. *ACS Earth Space Chem.* **2020**, *4* (11), 2171−2184.
(54) Rivera-Adorno, F. A.; Tomlin, J. M.; Fraund, M.; Morgan, E.; Laskin, M.; Moffet, R.; Laskin, A. Estimating Viscosity of Individual Substrate-Deposited Particles from Measurements of Their Height-to-Width Ratios. *Aerosol Sci. Technol.* **2024**, *58* (4), 401−410.
(55) Moffet, R. C.; Henn, T.; Laskin, A.; Gilles, M. K. Automated Chemical Analysis of Internally Mixed Aerosol Particles Using X-Ray Spectromicroscopy at the Carbon K-Edge. *Anal. Chem.* **2010**, *82* (19), 7906−7914.
(56) Fraund, M.; Park, T.; Yao, L.; Bonanno, D.; Pham, D. Q.; Moffet, R. C. Quantitative Capabilities of STXM to Measure Spatially Resolved Organic Volume Fractions of Mixed Organic/Inorganic Particles. *Atmos. Meas. Technol.* **2019**, *12* (3), 1619−1633.
(57) Knopf, D. A.; Alpert, P. A.; Wang, B.; O'Brien, R. E.; Kelly, S. T.; Laskin, A.; Gilles, M. K.; Moffet, R. C. Microspectroscopic Imaging and Characterization of Individually Identified Ice Nucleating Particles from a Case Field Study. *J. Geophys. Res. Atmos.* **2014**, *119* (17), 10365−10381.
(58) Henke, B. L.; Gullikson, E. M.; Davis, J. C. X-Ray Interactions: Photoabsorption, Scattering, Transmission, and Reflection at E = 50−30,000 eV, Z = 1−92. *Atomic Data and Nuclear Data Tables* **1993**, *54* (2), 181−342.
(59) Petters, M. D.; Kreidenweis, S. M. A Single Parameter Representation of Hygroscopic Growth and Cloud Condensation Nucleus Activity. *Atmos. Chem. Phys.* **2007**, *7* (8), 1961−1971.
(60) Kreidenweis, S. M.; Asa-Awuku, A. Aerosol Hygroscopicity: Particle Water Content and Its Role in Atmospheric Processes. *Treatise on Geochemistry*; Elsevier, 2014; pp 331−361. DOI: 10.1016/B978-0-08-095975-7.00418-6.
(61) Bougiatioti, A.; Bezantakos, S.; Stavroulas, I.; Kalivitis, N.; Kokkalis, P.; Biskos, G.; Mihalopoulos, N.; Papayannis, A.; Nenes, A. Biomass-Burning Impact on CCN Number, Hygroscopicity and Cloud Formation during Summertime in the Eastern Mediterranean. *Atmos. Chem. Phys.* **2016**, *16* (11), 7389−7409.
(62) Riemer, N.; West, M. Quantifying Aerosol Mixing State with Entropy and Diversity Measures. *Atmos. Chem. Phys.* **2013**, *13* (22), 11423−11439.
(63) Pósfai, M.; Simonics, R.; Li, J.; Hobbs, P. V.; Buseck, P. R. Individual Aerosol Particles from Biomass Burning in Southern Africa: 1. Compositions and Size Distributions of Carbonaceous Particles. *J. Geophys. Res.* **2003**, *108* (D13), 2002JD002291.
(64) Li, J.; Pósfai, M.; Hobbs, P. V.; Buseck, P. R. Individual Aerosol Particles from Biomass Burning in Southern Africa: 2, Compositions and Aging of Inorganic Particles. *J. Geophys. Res.* **2003**, *108* (D13), 2002JD002310.
(65) Aurela, M.; Beukes, J. P.; Van Zyl, P.; Vakkari, V.; Teinilä, K.; Saarikoski, S.; Laakso, L. The Composition of Ambient and Fresh Biomass Burning Aerosols at a Savannah Site, South Africa. *S. Afr. J. Sci.* **2016**, *112* (5/6), 8.
(66) Zhai, J.; Lu, X.; Li, L.; Zhang, Q.; Zhang, C.; Chen, H.; Yang, X.; Chen, J. Size-Resolved Chemical Composition, Effective Density, and Optical Properties of Biomass Burning Particles. *Atmos. Chem. Phys.* **2017**, *17* (12), 7481−7493.
(67) Zauscher, M. D.; Wang, Y.; Moore, M. J. K.; Gaston, C. J.; Prather, K. A. Air Quality Impact and Physicochemical Aging of Biomass Burning Aerosols during the 2007 San Diego Wildfires. *Environ. Sci. Technol.* **2013**, *47* (14), 7633−7643.
(68) Jing, B.; Peng, C.; Wang, Y.; Liu, Q.; Tong, S.; Zhang, Y.; Ge, M. Hygroscopic Properties of Potassium Chloride and Its Internal Mixtures with Organic Compounds Relevant to Biomass Burning Aerosol Particles. *Sci. Rep.* **2017**, *7* (1), 43572.
(69) Hand, J. L.; Malm, W. C.; Laskin, A.; Day, D.; Lee, T.; Wang, C.; Carrico, C.; Carrillo, J.; Cowin, J. P.; Collett, J.; Iedema, M. J. Optical, Physical, and Chemical Properties of Tar Balls Observed during the Yosemite Aerosol Characterization Study. *J. Geophys. Res.* **2005**, *110* (D21), D21210.
(70) Adachi, K.; Buseck, P. R. Atmospheric Tar Balls from Biomass Burning in Mexico. *J. Geophys. Res.* **2011**, *116* (D5), D05204.
(71) Pósfai, M.; Gelencsér, A.; Simonics, R.; Arató, K.; Li, J.; Hobbs, P. V.; Buseck, P. R. Atmospheric Tar Balls: Particles from Biomass and Biofuel Burning. *J. Geophys. Res.* **2004**, *109* (D6), D06213.

(72) Stöber, W. A Note on the Aerodynamic Diameter and the Mobility of Non-Spherical Aerosol Particles. *J. Aerosol Sci.* **1971**, *2* (4), 453−456.
(73) Laskin, A.; Cowin, J. P. Automated Single-Particle SEM/EDX Analysis of Submicrometer Particles down to 0.1 Mm. *Anal. Chem.* **2001**, *73* (5), 1023−1029.
(74) Ivosevic, M.; Cairncross, R. A.; Knight, R. 3D Predictions of Thermally Sprayed Polymer Splats: Modeling Particle Acceleration, Heating and Deformation on Impact with a Flat Substrate. *Int. J. Heat Mass Transfer* **2006**, *49* (19−20), 3285−3297.
(75) Esmen, N. A.; Ziegler, P.; Whitfield, R. The Adhesion of Particles upon Impaction. *J. Aerosol Sci.* **1978**, *9* (6), 547−556.
(76) Xie, Q.; Halpern, E. R.; Zhang, J.; Shrivastava, M.; Zelenyuk, A.; Zaveri, R. A.; Laskin, A. Volatility Basis Set Distributions and Viscosity of Organic Aerosol Mixtures: Insights from Chemical Characterization Using Temperature-Programmed Desorption-Direct Analysis in Real-Time High-Resolution Mass Spectrometry. *Anal. Chem.* **2024**, *96* (23), 9524−9534.
(77) Shiraiwa, M.; Ammann, M.; Koop, T.; Pöschl, U. Gas Uptake and Chemical Aging of Semisolid Organic Aerosol Particles. *Proc. Natl. Acad. Sci. U.S.A.* **2011**, *108* (27), 11003−11008.
(78) Sedlacek, A. J., III; Buseck, P. R.; Adachi, K.; Onasch, T. B.; Springston, S. R.; Kleinman, L. Formation and Evolution of Tar Balls from Northwestern US Wildfires. *Atmos. Chem. Phys.* **2018**, *18* (15), 11289−11301.
(79) Baboomian, V. J.; Crescenzo, G. V.; Huang, Y.; Mahrt, F.; Shiraiwa, M.; Bertram, A. K.; Nizkorodov, S. A. Sunlight Can Convert Atmospheric Aerosols into a Glassy Solid State and Modify Their Environmental Impacts. *Proc. Natl. Acad. Sci. U.S.A.* **2022**, *119* (43), No. e2208121119.
(80) Hettiyadura, A. P. S.; Garcia, V.; Li, C.; West, C. P.; Tomlin, J.; He, Q.; Rudich, Y.; Laskin, A. Chemical Composition and Molecular-Specific Optical Properties of Atmospheric Brown Carbon Associated with Biomass Burning. *Environ. Sci. Technol.* **2021**, *55* (4), 2511−2521.
(81) Riemer, N.; Ault, A. P.; West, M.; Craig, R. L.; Curtis, J. H. Aerosol Mixing State: Measurements, Modeling, and Impacts. *Rev. Geophys.* **2019**, *57* (2), 187−249.
(82) Petters, M. D.; Carrico, C. M.; Kreidenweis, S. M.; Prenni, A. J.; DeMott, P. J.; Collett, J. L.; Moosmüller, H. Cloud Condensation Nucleation Activity of Biomass Burning Aerosol. *J. Geophys. Res.* **2009**, *114* (D22), D22205.
(83) Psichoudaki, M.; Nenes, A.; Florou, K.; Kaltsonoudis, C.; Pandis, S. N. Hygroscopic Properties of Atmospheric Particles Emitted during Wintertime Biomass Burning Episodes in Athens. *Atmos. Environ.* **2018**, *178*, 66−72.
(84) Pham, D. Q.; O'Brien, R.; Fraund, M.; Bonanno, D.; Laskina, O.; Beall, C.; Moore, K. A.; Forestieri, S.; Wang, X.; Lee, C.; Sultana, C.; Grassian, V.; Cappa, C. D.; Prather, K. A.; Moffet, R. C. Biological Impacts on Carbon Speciation and Morphology of Sea Spray Aerosol. *ACS Earth Space Chem.* **2017**, *1* (9), 551−561.
(85) Zeng, L.; Sullivan, A. P.; Washenfelder, R. A.; Dibb, J.; Scheuer, E.; Campos, T. L.; Katich, J. M.; Levin, E.; Robinson, M. A.; Weber, R. J. Assessment of Online Water-Soluble Brown Carbon Measuring Systems for Aircraft Sampling. *Atmos. Meas. Technol.* **2021**, *14* (10), 6357−6378.
(86) Andreae, M. O.; Gelencser, A. Black Carbon or Brown Carbon? The Nature of Light-Absorbing Carbonaceous Aerosols. *Atmos. Chem. Phys.* **2006**, *6*, 3131−3148.
(87) Laskin, A.; Laskin, J.; Nizkorodov, S. A. Chemistry of Atmospheric Brown Carbon. *Chem. Rev.* **2015**, *115* (10), 4335−4382.
(88) Saleh, R. From Measurements to Models: Toward Accurate Representation of Brown Carbon in Climate Calculations. *Curr. Pollution Rep.* **2020**, *6* (2), 90−104.
(89) Li, X.; Chen, Y.; Bond, T. C. Light Absorption of Organic Aerosol from Pyrolysis of Corn Stalk. *Atmos. Environ.* **2016**, *144*, 249−256.
(90) Browne, E. C.; Zhang, X.; Franklin, J. P.; Ridley, K. J.; Kirchstetter, T. W.; Wilson, K. R.; Cappa, C. D.; Kroll, J. H. Effect of Heterogeneous Oxidative Aging on Light Absorption by Biomass Burning Organic Aerosol. *Aerosol Sci. Technol.* **2019**, *53* (6), 663−674.

https://doi.org/10.1021/acsestair.4c00242
ACS EST Air 2025, 2, 508−521